



## Science Arts & Métiers (SAM)

is an open access repository that collects the work of Arts et Métiers ParisTech researchers and makes it freely available over the web where possible.

This is an author-deposited version published in: <http://sam.ensam.eu>  
Handle ID: <http://hdl.handle.net/10985/10145>

### To cite this version :

L. SCIACOVELLI, Paola CINNELLA - Numerical Study of Multistage Transcritical Organic Rankine Cycle Axial Turbines - Journal of Engineering for Gas Turbines and Power - Vol. 082604-8, n°136, p.082604-1 - 2014

Any correspondence concerning this service should be sent to the repository

Administrator : [archiveouverte@ensam.eu](mailto:archiveouverte@ensam.eu)

# Numerical study of multistage transcritical ORC axial turbines

**L. Sciacovelli**

DynFluid Laboratory  
Arts et Métiers ParisTech  
151, Boulevard de l'Hôpital, 75013, Paris, France  
Email: luca.sciacovelli@ensam.eu

**P. Cinnella**

DynFluid Laboratory  
Arts et Métiers ParisTech  
151, Boulevard de l'Hôpital, 75013, Paris, France  
Email: paola.cinnella@ensam.eu

## ABSTRACT

*Transonic flows through axial, multi-stage, transcritical ORC turbines, are investigated by using a numerical solver including advanced multiparameter equations of state and a high-order discretization scheme. The working fluids in use are the refrigerants R134a and R245fa, classified as dense gases due to their complex molecules and relatively high molecular weight. Both inviscid and viscous numerical simulations are carried out to quantify the impact of dense gas effects and viscous effects on turbine performance. Both supercritical and subcritical inlet conditions are studied for the considered working fluids. In the former case, flow across the turbine is transcritical, since turbine output pressure is subcritical. Numerical results show that, due to dense gas effects characterizing the flow at supercritical inlet conditions, supercritical ORC turbines enable, for a given pressure ratio, a higher isentropic efficiency than subcritical turbines using the same working fluid. Moreover, for the selected operating conditions, R134a provides a better performance than R245fa.*

## Nomenclature

- a Speed of sound
- $C_f$  Friction coefficient
- $c_p$  Specific heat capacity at constant pressure
- $c_v$  Specific heat capacity at constant volume
- e Internal energy
- E Total internal energy
- f Flux

$H$  Total enthalpy  
 $\bar{I}$  Unit tensor  
 $p$  Pressure  
 $Pr$  Prandtl number  
 $q$  Actual order of convergence  
 $\mathbf{q}$  Heat flux vector  
 $R$  Universal gas constant  
 $r$  Grid refinement ratio  
 $s$  Entropy  
 $T$  Temperature  
 $v$  Specific volume  
 $\mathbf{v}$  Flow velocity vector  
 $\mathcal{V}$  Control Volume  
 $\partial\mathcal{V}$  Boundary of the control volume  
 $\mathbf{w}$  Conservative variables vector  
 $Z$  Compressibility factor  
 $\gamma$  Specific heat ratio  
 $\Gamma$  Fundamental Derivative of Gas Dynamics  
 $\delta$  Reduced density  
 $\eta$  Isentropic efficiency  
 $\kappa$  Thermal Conductivity  
 $\mu$  Dynamic Viscosity  
 $\rho$  Density  
 $\sigma$  Dipole moment  
 $\sigma_r$  Dimensionless dipole moment  
 $\tau$  Inverse reduced temperature  
 $\bar{\tau}$  Viscous stress tensor  
 $\Phi$  Helmholtz free energy  
 $\omega$  Acentric factor  
 $\bar{\Omega}$  Angular velocity  
*Subscript*  
 $\infty$  ideal-gas state  
 $c$  critical value

## 1 Introduction

Organic Rankine Cycles (ORCs) have been largely studied for their relatively high efficiency [1] for low-temperature energy conversion cycles. For instance, the ORC technology has been applied in geothermal [2] and biomass [3] fired power plants, bottoming cycles for combined cycle power plants [4], solar reverse osmosis desalination plants, and others, allowing efficiency improvements, reduction of the cycle size and production in modular units. Recently, many studies have demonstrated that supercritical ORCs (SRCs), i.e., ORCs in which heat is supplied at a pressure greater than the liquid/vapor critical point pressure, have an even better potential, since they enable a higher recovery efficiency for a simplified cycle architecture [5]. In contrast to a conventional ORC, the working fluid of a SRC is heated directly from liquid state into supercritical state, bypassing the two-phase region, which allows it to have a better thermal match with the heat source, resulting in less exergy destruction. The choice of working fluids is of key importance for the performance of SRCs. Carbon dioxide has been studied as the working fluid of SRCs by a number of investigators [5–7]. However, the CO<sub>2</sub>-based SRC operates under pressures as high as 16 MPa, while condensing the carbon dioxide is also a challenge due to its low condensation temperature. Beside carbon dioxide, fluids such as hydrocarbons and refrigerants R134a, R227ea, R236fa and R245fa have also been studied as the working fluids in SRCs, and the results showed that the thermal efficiency could improve by about 10%, compared to the same working fluids used in subcritical ORCs. [5]

Most studies about SRCs deal with global thermodynamic efficiency considerations. However, cycle efficiency strongly depends on cycle components. Specifically, the isentropic efficiency of the turbine has a strong impact on the overall cycle efficiency. In SRCs, the turbine typically works at transcritical conditions, since the pressure is supercritical at turbine inlet and subcritical at the outlet. A significant exception is represented by supercritical CO<sub>2</sub> cycles, where the whole expansion happens at supercritical conditions.

In this work we carry out a numerical investigation of flows through transcritical axial multi-stage ORC turbines, using a numerical code with a high-order discretization scheme. Subcritical turbines are also considered, and the impact of choosing supercritical or subcritical inlet conditions in terms of isentropic efficiency is investigated. Two working fluids are studied, namely, the refrigerants R134a and R245fa. These two fluids have been widely used in ORC plants [2,8] due to their excellent thermal and chemical stability and low flammability. Furthermore, their critical temperatures and pressures, much lower than those of water, make them particularly suitable for low-temperature applications. Both organic fluids are characterized by complex molecules and moderate molecular weights, and can be classified as dense gases according to [9]. Furthermore, a turbine using carbon dioxide (CO<sub>2</sub>) as the working fluid is also considered for comparison. Thermodynamic properties of the fluids under investigation are listed in Tab. 1. At thermodynamic conditions typical of a SRC turbine, the ideal-gas approximation is no longer valid and real-gas effects become significant. For this reason, advanced multiparameter equations of state are required to model the thermodynamic behavior of the working fluids accurately.

Several recent studies have addressed real-gas flow over airfoils or turbine cascades. Simulations of viscous turbulent real gas flows through a nozzle of a radial ORC turbine were performed in [10]. A study of the influence of thermodynamic models on turbine simulation results by means of 2D inviscid simulations through an ORC turbine nozzle blade has been presented in [11]. Also, a numerical investigation of dense-gas effects in turbine cascades by means of several equations of

state was presented in [12]. More recently, numerical results have been presented for a radial ORC turbine stage [13].

The dynamics of dense gases may differ significantly from that of perfect gases. The qualitative behavior of compressible flows depends on the value of a thermodynamic parameter, the so-called fundamental derivative of Gas Dynamics  $\Gamma$  [14]:

$$\Gamma = \frac{v^3}{2a} \left( \frac{\partial^2 p}{\partial^2 v} \right)_s = 1 + \frac{\rho}{a} \left( \frac{\partial a}{\partial \rho} \right)_s \quad (1)$$

where  $\rho$  and  $s$  are the fluid density and entropy, and  $a = [-v^2(\partial p/\partial v)_s]^{1/2}$  is the speed of sound.  $\Gamma$  represents a measure of the rate of change for the local propagation speed of weak disturbances of pressure. The value of  $\Gamma$  for perfect gases, i.e. gases satisfying the ideal gas law and the condition of constant specific heats, is  $\Gamma = (\gamma + 1)/2$ . Since for thermodynamic stability reasons, the value of the specific heat ratio  $\gamma$  is always greater than unity,  $\Gamma > 1$ . This also holds for most fluids characterized by light weights and simple molecules. For more complex fluids,  $\Gamma$  may become lower than unity. In this case, flows undergoing isentropic perturbations exhibit a different sound-speed behavior, according to whether  $\Gamma$  is higher or lower than unity: when  $\Gamma > 1$ , the speed of sound drops in isentropic expansions and grows in isentropic compressions, like in "common" gases; an opposite behavior is obtained when  $\Gamma < 1$ . Thermodynamic regions with  $\Gamma$  lower than unity are observed for molecularly complex fluids at temperatures and pressures close to saturation conditions. Both the organic working fluids considered in this study may exhibit dense gas effects in the thermodynamic region of interest for SRC turbine expanders.

Another important difference between light and dense gases resides in the viscous effects, since the viscosity of dense gases has a complex behavior, intermediate between that of liquids, which tends to decrease with increasing temperature, and that of gases, with an opposite variation. Furthermore, the dynamic viscosity  $\mu$  and the thermal conductivity  $\kappa$  cannot be considered independent from temperature and pressure in the real gas regions. In a similarly way, the approximation of constant Prandtl number  $Pr$  does not hold any more: its behavior tends to be controlled by variations of the specific heat  $c_p$ , the thermal conductivity showing variations with temperature and pressure similar to viscosity. In the supercritical regime, where  $c_p$  becomes large, strong variations of  $Pr$  can be observed, in contrast with the perfect gas case. The viscous behavior of dense gas flows has been discussed in [15].

The paper is organized as follows. First, we briefly recall the governing equations and thermodynamic models in use. Then we describe the ORC turbines under investigation and comment on the numerical setup. Finally, several inviscid and viscous simulations of transcritical and subcritical flows through the turbines are carried out : the impact of the working fluid on turbine performance is investigated, with focus on the entropy losses associated to shock wave formation and viscous effects. Conclusions are drawn about the suitability of the different working fluids for the present target application.

## 2 Governing Equations and Flow solver

Dense gas flows are governed by the equilibrium equations for non-reacting flows. In this study we consider the Reynolds-Averaged Navier-Stokes equations, written in integral form for a control volume  $\mathcal{V}$  with boundary  $\partial\mathcal{V}$ :

$$\int_{\mathcal{V}} \mathbf{w} d\mathcal{V} + \oint_{\partial\mathcal{V}} (\mathbf{f}^e - \mathbf{f}^v) \cdot \mathbf{n} dS = \mathbf{S} \quad (2)$$

with

$$\mathbf{w} = \begin{bmatrix} \rho \\ \rho\mathbf{v} \\ \rho E \end{bmatrix}, \quad \mathbf{f}^e = \begin{bmatrix} \rho\mathbf{v} \\ \rho\mathbf{v}\mathbf{v} + p\bar{\mathbf{I}} \\ \rho\mathbf{v}H \end{bmatrix}, \quad \mathbf{f}^v = \begin{bmatrix} 0 \\ \bar{\bar{\tau}} + \bar{\bar{\tau}}_R \\ (\bar{\bar{\tau}} + \bar{\bar{\tau}}_R) \cdot \mathbf{v} - \mathbf{q} - \mathbf{q}_R \end{bmatrix}, \quad \mathbf{S} = \begin{bmatrix} 0 \\ -\rho\bar{\bar{\Omega}} \times \mathbf{v} \\ 0 \end{bmatrix} \quad (3)$$

where  $\mathbf{w}$  is the conservative variable vector,  $\mathbf{n}$  the outer normal to  $\partial\mathcal{V}$ ,  $\mathbf{f}^e$  and  $\mathbf{f}^v$  respectively the inviscid and viscous part of the flux density, and  $\mathbf{S}$  a source term accounting for apparent forces; in the above,  $\mathbf{v}$  is the velocity vector,  $E$  the specific total energy,  $H = E + p/\rho$  the specific total enthalpy,  $p$  the pressure,  $\bar{\mathbf{I}}$  the unit tensor,  $\bar{\bar{\tau}} = 2\mu(\nabla\mathbf{v} + \nabla\mathbf{v}^T) - \frac{2}{3}\mu(\nabla \cdot \mathbf{v})\bar{\mathbf{I}}$  the viscous stress tensor,  $\bar{\bar{\tau}}_R$  is the Reynolds stress tensor, used to model the effect of turbulent fluctuation on the average field,  $\bar{\bar{\Omega}}$  the angular velocity,  $\mathbf{q} = -\kappa\nabla T$  is the heat flux vector, with  $T$  the absolute temperature, and  $\mathbf{q}_R$  the turbulent heat flux. The preceding equations are completed by a thermal and a caloric equation of state (EOS), which allow computing respectively the pressure and the internal energy from density and temperature:

$$p = p(\rho(\mathbf{w}), T(\mathbf{w})) \quad (4)$$

$$e = e(\rho(\mathbf{w}), T(\mathbf{w})) \quad (5)$$

and by thermodynamic models relating the dynamic viscosity  $\mu$  and the thermal conductivity  $\kappa$  to the temperature and pressure values of the gas,  $\mu = \mu(T, p)$ ,  $\kappa = \kappa(T, p)$ . The caloric equation of state must satisfy the compatibility relation:

$$e = e(\rho(\mathbf{w}), T(\mathbf{w})) = e_r + \int_{T_r}^T c_{v,\infty}(T') dT' - \int_{p_r}^p \left[ T \left( \frac{\partial p}{\partial T \rho} - p \right) \right] \frac{dp'}{\rho'^2} \quad (6)$$

where  $c_{v,\infty}$  is the ideal-gas specific heat at constant volume, the prime-subscripted quantities are auxiliary integration variables, and the subscript  $r$  indicates a reference state. The caloric equation of state is fully determined by specifying a variation law for  $c_{v,\infty}$  in terms of the temperature.

Reynolds stress are modelled by an eddy viscosity model, as discussed in 2.3, whereas the turbulent heat flux is approximated by using a turbulent Fourier law.

For inviscid flow simulations, we solve the Euler equations, obtained from Eq. 2 by setting the viscous flux  $\mathbf{f}^v$  to zero.

## 2.1 Equations of state (EOS)

The gas response is modelled through multiparameter EOS based on the Helmholtz free energy  $\Phi$ , which represent the most accurate available models for the fluids of interest in thermodynamic regions close to the critical point and the saturation curves. These EOS are written in the form proposed by Setzmann and Wagner [16]:  $\Phi(\delta, \tau) = \Phi^0(\delta, \tau) + \Phi^r(\delta, \tau)$ . They use a reduced form (variables normalized with respect to critical-point properties) and are composed by an ideal-gas part,  $\Phi^0$ , function of the ideal-gas isobaric heat capacity:

$$\Phi^0(\delta, \tau) = \ln \delta + a_1 \ln \tau + \sum_{m=1}^{M_1} a_m \tau^{j_m} + \sum_{m=M_1+1}^{M_2} a_m \ln[1 - \exp(-u_m \tau)] \quad (7)$$

and by a residual term,  $\Phi^r$ , that takes into account real-gas corrections:

$$\Phi^r(\delta, \tau) = \sum_{m=M_2+1}^{M_3} a_m \delta^{i_m} \tau^{j_m} + \sum_{m=M_3+1}^{M_4} a_m \delta^{i_m} \tau^{j_m} \exp(-\delta^{k_m}) + \sum_{m=M_4+1}^{M_5} a_m \delta^{i_m} \tau^{j_m} \exp[-\alpha_m (\delta - \epsilon_m)^2 - \beta_m (\tau - \gamma_m)^2] \quad (8)$$

where  $\delta = \rho/\rho_c$  is the reduced density and  $\tau = T_c/T$  is the inverse reduced temperature. The last sum on the right-hand side of (8) accounts for critical point correction terms. The number of polynomial and exponential terms and the values of coefficients and exponents is chosen in order to obtain the best possible fit to experimental data by means of an optimization algorithm described in [16]. A in-house flow solver has been equipped with reference EOS available for R134a [17] and CO<sub>2</sub> [18].

For R245fa no reference EOS is available, thus we adopt the short technical multiparameter EOS proposed by Span and Wagner [19]. This kind of EOS, also expressed in the Helmholtz explicit functional form, conserves the same formulation

for the ideal part, whereas the residual part is written in the more compact form:

$$\begin{aligned} \Phi^r(\delta, \tau) = & n_1 \delta \tau^{0.25} + n_2 \delta \tau^{1.25} + n_3 \delta \tau^{1.5} + \\ & + n_4 \delta^3 \tau^{0.25} + n_5 \delta^7 \tau^{0.875} + n_6 \delta \tau^{2.375} \exp(-\delta) + \\ & + n_7 \delta^2 \tau^{2.0} \exp(-\delta) + n_8 \delta^5 \tau^{2.125} \exp(-\delta) + \\ & + n_9 \delta \tau^{3.5} \exp(-\delta^2) + n_{10} \delta \tau^{6.5} \exp(-\delta^2) + \\ & + n_{11} \delta^4 \tau^{4.75} \exp(-\delta^2) + n_{12} \delta^2 \tau^{12.5} \exp(-\delta^3) \end{aligned} \quad (9)$$

where  $n_1, \dots, n_{12}$  are substance-specific coefficients. These have been fitted for classes of polar fluids and nonpolar fluids simultaneously. The bell-shaped terms that take into account corrections in the critical region are not present, since they depend on the specific fluid. As a result, this EOS is less accurate than a reference EOS. Nonetheless, compared to other multi-parameter EOS, the Span-Wagner EOS has by far superior accuracy and numerical stability [20]. Both kinds of EOS described above require an ancillary equation for the calculation of caloric properties. The ideal gas contribution to the specific heat at constant pressure depends on the reduced temperature and it is approximated with Einstein-like form functions for R245fa and carbon dioxide, specifically:

$$\frac{c_{p,\infty}(\tau)}{R} = 1 + c_1 + \sum_{i=1}^5 v_k (u_k \tau)^2 \frac{\exp(u_k \tau)}{[\exp(u_k \tau) - 1]^2} \quad (10)$$

whereas for R134a a polynomial function is used to fit the experimental data:

$$\frac{c_{p,\infty}(\tau)}{R} = c_1 + c_2 \tau^{-1/2} + c_3 \tau^{-3/4} \quad (11)$$

The coefficient  $c_1, c_2, c_3, v_k$  and  $u_k$  are fluid dependent and are provided in [17–19].

## 2.2 Viscosity and thermal conductivity models

The dynamic viscosity and thermal conductivity models used are those described in [21, 22]. The dynamic viscosity law, expressed in  $\mu\text{Pa}$ , reads:

$$\mu = 40.875 \frac{F_c M_w^{1/2} T^{1/2}}{V_c^{2/3} \Omega_v} \quad (12)$$



where  $M_w$  is the molecular weight (in g/mol) and  $V_c$  the critical volume in  $\text{cm}^3/\text{mol}$ .  $F_c$  is a coefficient given by  $F_c = 1 - 0.2756\omega + 0.059035\sigma_r^4 + \xi$ , where  $\omega$  is the acentric factor,  $\xi$  is a special correction for highly polar substances and  $\sigma$  is the dimensionless dipole moment:

$$\sigma_r = 131.3 \frac{\sigma}{(V_c T_c)^{1/2}} \quad (13)$$

$\Omega_v$  is the collision integral, written:

$$\Omega_v = A(T^*)^{-B} + C \exp(-DT^*) + E \exp(-FT^*) \quad (14)$$

with  $T^* = 1.2593/\tau$ ,  $A = 1.16145$ ,  $B = 0.14874$ ,  $C = 0.52487$ ,  $D = 0.7732$ ,  $E = 2.16178$ ,  $F = 2.43787$ . The thermal conductivity  $\kappa$  is obtained from:

$$\frac{\kappa M'_w}{\mu c_v} = \frac{3.75\Psi}{c_v/R} \quad (15)$$

being  $M'_w$  the molecular weight,  $c_v$  the specific heat at constant volume,  $R$  the universal gas constant and  $\Psi$  a coefficient given by:

$$\Psi = 1 + \alpha \frac{0.215 + 0.28288\alpha - 1.061\beta + 0.26665\Xi}{0.6366 + \beta\Xi + 1.061\alpha\beta} \quad (16)$$

with  $\alpha = c_v/\mathfrak{R} - 3/2$ ,  $\beta = 0.7862 - 0.1709\omega + 1.3168\omega^2$  and  $\Xi = 2.0 + 10.5/\tau^2$ .

### 2.3 Turbulence models

Since typical Reynolds number for flows through turbine cascades are in the range  $10^5$ - $10^6$ , turbulence effects cannot be neglected. The following simulations of turbulent dense gas flows are based on two working hypotheses. Firstly, the working thermodynamic conditions in the turbine cascades are sufficiently far from the critical point of the selected fluids, so that very huge variations of the fluid compressibility and specific heat can be neglected. In such a way, the density fluctuations remain small and the turbulent structures are not heavily affected by dense gas effects. Secondly, the mean flow behavior can be described by means of compressible Reynolds-averaged Navier-Stokes equations equipped with an eddy viscosity turbulence model, at least for equilibrium boundary layers. Furthermore, it is possible to model the turbulent heat transfer through a ‘‘turbulent Fourier law’’, as it is of common practice for perfect gases, in which the turbulent thermal conductivity

is computed by means of a turbulent Prandtl number, assumed constant and  $O(1)$  throughout the flows.

In this work, two turbulence models are considered: the simple algebraic model of Baldwin and Lomax [23] and the one-equation Spalart-Allmaras [24] transport model.

## 2.4 Flow solver

The governing equations are discretized using a cell-centered finite volume scheme of third-order accuracy for structured multi-block meshes, which allows the computation of flows governed by arbitrary EOS [25]. The scheme is obtained by correcting the dispersive error of the classical second-order-accurate Jameson's scheme [26]. To preserve the high accuracy on non-Cartesian grids, the numerical fluxes are constructed by using weighted discretization formulas, which take into account the mesh deformations [27]. This ensures to achieve third-order accuracy on moderately distorted meshes and second-order accuracy at least on highly deformed mesh. The equations are then integrated in time using a four-stage Runge-Kutta scheme. Local time stepping, implicit residual smoothing and multi-grid acceleration are used in order to drive the solution to the steady state. The accuracy of the numerical solver, already demonstrated in previous works [28, 29], will not be further investigated.

## 3 Numerical setup

The geometrical configurations under investigations are axial reaction turbines with a variable number of stages according to the working fluid in use. The reaction degree is fixed to 0.5. The rotational speed is fixed at 3000 RPM to allow direct coupling with the alternator. The same airfoil shapes are used for both stator and rotor wheels. The number of stages and their relative average radius were calculated in the pre-design phase by taking into account the operating conditions (inlet total conditions, mass flow and pressure ratio), as well as cost and system complexity considerations.

A three-stage turbine working with refrigerant R245fa was designed to work at subcritical nominal conditions, and four-stage turbines, designed for supercritical nominal conditions, are used with fluids R134a and CO<sub>2</sub>. The turbine inlet conditions were chosen in order to maximize the performance of the ORC cycle, such as the heat recovery efficiency, the surface area of the heat exchangers, the total thermal power exchanged, and the available enthalpy fall in turbine. To check the impact of different working fluids on the overall performance of a given turbine, the subcritical turbine was also tested with R134a, and the supercritical one with R245fa. To this aim, the same reduced conditions were imposed at turbine inlet for both fluids, while keeping the same expansion ratio for each turbine stage.

Numerical simulations were also carried out for a SRC using carbon dioxide as the working fluid. In the latter case, subcritical inlet conditions were not suitable, and therefore only fully supercritical conditions were tested. The ideal expansion curves in the  $T - s$  diagram are shown in Fig. 1, 2, 3. The different turbine configurations under investigation are described in Tab. 2. The prefix SUB- and SUP- are used to indicate respectively subcritical and supercritical inlet nominal conditions. The total expansion ratio for the SUPCO<sub>2</sub> case is relatively low with respect to the other working fluids, due to its higher critical pressure. Nevertheless, the higher pressure jump through each stage ensures an enthalpy fall similar to the other supercritical cases. Both inviscid and viscous simulations were performed for each case. Inviscid simulations only account

for losses due to shock waves, but they represent a suitable model for a qualitative study of the impact of dense gas effects on the computed flow fields. Then, viscous turbulent simulations are carried out to quantify viscous losses, and the impact of viscous effects on the overall flow behaviour.

For inviscid simulations, each blade vane is discretized by means of a C-shaped grid composed by  $384 \times 48$  cells (see Fig. 4), with a first cell height of the order of  $10^{-3}$  times the axial chord. For viscous computations, we use grids made of  $384 \times 64$  cells with an average  $y^+$  for near-wall cells of approximately 1. A grid refinement study is presented in the next Section. Thanks to azimuthal periodicity, the computational domain is reduced to a single blade passage per wheel, with periodicity conditions imposed at inter-blade boundaries. A mixing plane condition is imposed at stator/rotor interfaces. Characteristic conditions based on the conservation of Riemann invariants are applied at the inlet and outlet boundaries. As a common practice for turbomachines, the stagnation temperature and pressure, as well as the flow direction, are imposed at turbine inlet. At the outlet, being the flow subsonic, only static pressure is imposed, and all of the other quantities are extrapolated from the inner cells. For viscous flows, an adiabatic wall conditions is applied along the blades, whereas a no-slip wall condition based on second-order extrapolation of the pressure from the inner cells is used for inviscid flows.

### 3.1 Grid convergence study

To check independence of the numerical solution on the computational grid, a grid convergence study is carried out. For brevity, hereafter we consider only case SUPR134a of Table 2, but similar results are obtained for the other cases. For this case, all computational grids are made of eight C-shaped blocks, one for each blade included in the computational domain. For inviscid computations, we consider a set of three grids of increasing density, such that individual C-blocks are formed by  $192 \times 24$ ,  $384 \times 48$  and  $768 \times 96$  cells for the coarser, the medium, and the finer grid, respectively. The height of the first cell close to the wall is approximately  $2 \times 10^{-4}$ ,  $10^{-4}$ , and  $5 \times 10^{-5}$  times the axial chord, respectively.

First, we check the scheme convergence order following Roache's method [30], based on Richardson extrapolation. According to this method, considering three numerical solutions obtained on computational grids of increasing spacing with constant grid refinement ratio  $r$ , the actual order of convergence of the numerical solution to the exact one is given by

$$q = \frac{\ln\left(\frac{f_3 - f_2}{f_2 - f_1}\right)}{\ln(r)}$$

where  $f$  is a solution functional and indices 1,2,3 refers the the finest, medium and coarsest grid in use, respectively. The functional chosen for the present computations is the isentropic efficiency. The computed order of convergence is found to be 2.1, against a theoretical order of convergence of 3, the difference between the nominal and the actual order of convergence being due both to grid deformations and to the presence of shocks in the numerical solution. Using the actual order of convergence we computed the solution grid convergence index (CGI) on the finer and medium grid: this provides an estimate of how far the numerical solution is from asymptotic convergence. Grid convergence indices of 0.48 and 0.15 have been found for the medium and the finer grids, respectively, indicating that the solution is well within the asymptotic range already

on the medium grid.

Fig. 5 shows typical wall distributions of the pressure (normalized with the inlet pressure) on the three computational grids for the first stage rotor blade. It can be noticed that results obtained for the medium and finest grid are almost superposed. As a consequence, only the medium grid is used for the following inviscid computations.

In the viscous case we considered a set of two multiblock grids with a similar topology to that of the inviscid grids. Individual C blocks around each blade are composed of  $192 \times 32$  and  $384 \times 64$  cells, for the coarser and the finer grids, respectively. The actual order of convergence is assumed to be close, but slightly lower than that found in the inviscid case because of the second-order discretization used for the viscous terms. Precisely, based on previous experience [15], we assume  $q = 2$ . By using this value, the grid convergence index on the medium grid is found to be 0.41, showing that the solution on the medium grid is practically grid converged. Fig. 6 and Fig. 7 show wall distributions of the pressure and of the friction coefficient, respectively, for case SUPR134a. Differences between the two grids are below 2% so that only the medium grid is retained for the viscous computations presented in the following.

#### 4 Numerical simulation results

In the following we discuss numerical results obtained for the different turbine configurations of Tab. 2 in terms of both the overall characteristics of the flow fields generated through the machine and associated performance in terms of isentropic efficiency, computed as the real-to-ideal static enthalpy drop ratio.

As a preliminary general consideration we notice that, for all configurations under investigation the flow is high subsonic or transonic, so that shock waves are generated at upper surfaces of rotor blades for some turbine configurations and operating conditions. However, these shocks remain relatively weak, and the associated entropy losses small, compared to viscous losses.

To make that clear, stage efficiencies for the inviscid simulations are reported in Tab 3. Several considerations are in order: (1) the higher efficiencies are obtained when using carbon dioxide as working fluid; (2) as a general trend, supercritical turbines achieve higher efficiencies than subcritical turbines using the same working fluid; (3) for supercritical cases, stage efficiencies increase moving downstream through the turbine, while the opposite behavior is obtained using the same fluid with subcritical inlet conditions. This result is directly linked to dense gas effects, as it will be explained later in detail. Note that computed efficiencies are slightly lower than unity, even in cases for which the flow field is entirely shock-free and the flow is expected to be isentropic in the absence of viscous losses; this is due to the errors introduced by the numerical approximation of governing equations and boundary conditions.

Tables 4 and 5 present stage efficiencies obtained from viscous simulations based on the Baldwin-Lomax and the Spalart-Allmaras turbulence model, respectively. Results provided by the two models are quite similar, differences being below 1%. Viscous effects contribute to the overall losses for a much more significant amount than wave losses, and actually the computed isentropic efficiencies in the viscous case are about 10 percentage points lower than in the inviscid one. Nevertheless outside viscous boundary layers, which are thin and attached throughout the considered configurations, the general aspect of the numerical solution is quite the same both for viscous and inviscid computations, which also explains

strong similarities between solutions obtained by using the simple algebraic model of Baldwin and Lomax and the one equation Spalart-Allmaras model.

To further investigate the role of the physical model in use on the predicted flow fields and turbine performance, we focus for brevity on case SUPR134a, but similar considerations can be done for the other cases. Figs 8 and Fig. 9 show respectively the pressure and skin friction distributions along first stage rotor blades provided by different models. The wall pressure distributions provided by all models are fairly similar, showing that the main features of the flow are essentially related to inviscid effects. The Baldwin-Lomax model predicts lower wall pressure and friction coefficient magnitude at the blade suction side than Spalart-Allmaras, resulting in slightly higher isentropic efficiencies, but the results remain in very good qualitative agreement, and quantitative difference are below 2.5% for the pressure distribution and below 8% for the skin friction.

In the following we investigate in more detail the flow fields obtained for the different turbine configurations by means of viscous simulations based on the Baldwin-Lomax model.

Figs 10, 11, 12 and 13, show respectively iso-contours of the static pressure, Fundamental Derivative of Gas Dynamics  $\Gamma$ , relative Mach number  $M$ , and sound speed for case SUPR134a. The isocontours  $M = 1$  and  $\Gamma = 1$  are highlighted by dashed lines. Weak shock waves are created on the suction side of the rotor blades for all stages. The definition of  $\Gamma$  given in Eq. 1 implies that, for an almost isentropic transformation

$$\frac{da}{a} = (\Gamma - 1) \frac{d\rho}{\rho} \quad (17)$$

so that relative variations of the sound speed depend on relative variations of the density and on  $\Gamma$ . In the first stage the flow is transcritical and  $\Gamma$ , above unity at turbine inlet, quickly decreases, achieving a minimum downstream of the shock created in the first rotor. According to eq. (17) the speed of sound slightly decreases at the beginning of the expansion. Then, going from the second to the last stage,  $\Gamma$  increases again, but remains always lower than unity; consequently the sound speed increases as the expansion proceeds. Since flow velocity grows more slowly than the sound speed, the Mach number tends to decrease going downstream and the shock strength tends to weaken. This effect is reflected by the stage efficiencies, that from the first to the last stage, passing from 85.7 to 87.6 (see Tab. 4).

The expected impact of dense gas effects can be highlighted by examining the compressibility factor, defined as  $Z = pv/RT$ , at the turbine inlet and outlet. This parameter is identically equal to unity for an ideal gas, and it takes lower values as the thermodynamic behavior of the fluid departs from the ideal one. Compressibility factors for the different turbine configurations are listed in Tab. 2 for each simulation. For case SUPR134a, the compressibility factor at the turbine inlet is 0.55, and grows across the expansion up to 0.85 at the outlet. This indicates that the flow through the supercritical turbine undergoes stronger real gas effects at the beginning of the expansion, where the thermodynamic working conditions are closer to the critical region. The fundamental derivative, indeed, exhibits the strongest variations precisely in the first stage, where it reaches its minimum value, lower than one. Then, both the fundamental derivative and the compressibility factor

increase again when the flow moves downstream and the thermodynamic behavior becomes closer to the ideal one in the last stages.

For case SUPR245fa, results are shown in Figs 14, 16, and 15. The flow behaves similarly to case SUPR134a, but losses are higher. In this case,  $\Gamma$  is lower than unity through the entire turbine, starting from the first stage stator: as a consequence, the speed of sound always increases during the expansion. Dense gas effects are even stronger than case SUPR134a, because the values of  $\Gamma$  are globally lower, the minimum value being 0.75 against 0.82, and the maximum 1.05 against 1.1, as well as the compressibility factor, which ranges between 0.46 and 0.78 for this case. However, due to the different thermodynamic working conditions and the higher molecular weight (see Tab. 1), the speed of sound at the turbine inlet is significantly lower with respect to case SUPR134a (110 m/s for SUPR245fa, 130 m/s for SUPR134a), whereas flow speed is almost the same. Thus, the flow Mach number is higher for this configuration and shocks are stronger, spite of the considerable increase of the speed of sound through the expansion. This results in efficiencies roughly 5% lower than in the SUPR134a case.

For the subcritical configurations SUBR134a and SUBR245fa, the overall performance is lower than supercritical ones using the same working fluids. Lower isentropic efficiencies are due to the fact that the computed  $\Gamma$  value is nearly constant and close to unity. Results for the SUBR134a case are shown in Figs 20, 21, and 22. Only the first stage has a fundamental derivative value lower than unity, with a minimum of 0.975: the sound speed slightly increases through this stage, and then it remains approximately constant. Since the flow speed increases during the expansion, the Mach number and shock strength increase when moving downstream. A quite similar behavior is obtained for SUBR245fa (not shown for brevity). The compressibility factor values are comprised between 0.8 and 0.95, respectively at turbine inlet and outlet, demonstrating the absence of significant real gas effects, except for the first turbine stage. Hence, in the subcritical turbine the aerodynamic recovery effect due to the increase of the sound speed is lost, as well as the increase of the stage isentropic efficiencies, tightly related to shock strength. Things are made even worse by the fact that the subcritical turbine is designed for three stages instead of four; as a consequence, in spite of the lower overall pressure ratio, each stage processes a higher pressure ratio with respect to the supercritical turbine.

Finally, the ORC turbines are compared to a turbine using supercritical CO<sub>2</sub>. Results for case SUPCO<sub>2</sub> are shown in Figs 17, 18, and 19. The flow exhibits a completely different behavior with respect to the turbines using refrigerant fluids: it remains always subsonic and no shocks are formed. Being a light fluid, carbon dioxide has in fact a sound speed approximately double than that of R134a and R245fa. Thus, even if  $\Gamma$  is everywhere higher than unity (close to the perfect gas values at the turbine inlet) and the speed of sound decreases with fluid expansion, it is still high enough to prevent the flow from becoming supersonic. The low significance of real gas effects for this case is confirmed by inspection of the compressibility factor, which is almost constant and takes quite high values throughout the expansion. According to the present numerical results, CO<sub>2</sub> seems to be the most suitable working fluid to be employed in the ORC cycle under exam, at least as far as isentropic efficiency of the turbine is the primary concern. Nevertheless, the choice of an optimal working fluid for ORC turbines also involve other kinds of considerations, like economical and safety aspects. Supercritical CO<sub>2</sub> cycles involve average pressures of the order of 80 bars (the inlet pressure being about 150 bars in this case), which increases fabrication and installation costs. In addition, the high pressure drop per each stage, greater than 20 bars, could lead to

significant leakage flows with respect to the refrigerant fluid turbines, which are of course not taken into account in the present 2D simulations.

## 5 Conclusions

In this work, dense gas flows through supercritical multistage axial ORC turbines were investigated by means of an in-house dense gas numerical solver using a high-order finite volume scheme and equipped with accurate multiparameter equations of state based on Helmholtz free energy. Both inviscid and viscous simulations were performed in order to quantify the relative impact of dense gas and viscous effects on the flow behavior and the overall performance.

Calculations were carried out for 3 different supercritical turbine configurations. Two subcritical ORC turbines employing the same working fluids were also studied for comparison. The selected working fluids were R134a, R245fa and carbon dioxide, for each of which a state-of-the-art equation of state is available in the literature. Steady, two-dimensional numerical simulations were carried out to evaluate entropy losses associated to shock wave formation and viscous friction in the different cases. For viscous simulations, the Baldwin-Lomax and Spalart-Allmaras turbulence models were considered. Viscous effects do not modify the qualitative flow behavior with respect to the inviscid case. The impact of viscous losses on the isentropic efficiency is found to be almost fluid-independent, roughly constant in each stage and about 10 percentage points lower with respect to inviscid simulations, which take into account only wave losses. Since the boundary layers remain attached and there are no recirculation zones, both the considered turbulence models give quite similar results.

Comparisons between supercritical and subcritical configurations show that, for a given working fluid, the supercritical configurations, characterised by stronger dense gas effects slowing down the increase of the Mach number during the expansion, exhibit weaker shocks, and thus achieve higher isentropic efficiencies. This confirms, for the present more realistic configurations, results previously found in [15] and [12] for isolated airfoils and turbine cascades.

Moreover, comparisons between two candidate working fluids for a same turbine configuration show that refrigerant R134a tends to provide a better performance than R245fa in terms of isentropic efficiency. This can again be explained by the more favourable impact of dense gas effects on shock strength observed in R134a at the considered reduced conditions. Finally, comparisons of turbine configurations employing the above mentioned refrigerants against a turbine using supercritical CO<sub>2</sub> as the working fluid show that, due to its higher speed of sound, supercritical CO<sub>2</sub> leads, for a similar pressure ratio, to a fully subsonic flow instead of transonic flow observed for the ORC turbines (both for subcritical and supercritical configurations). In this sense, CO<sub>2</sub> provides an optimal fluid dynamic behavior in terms of wave losses. However, due to the much higher average pressures involved in supercritical CO<sub>2</sub> cycles, economic and safety aspects may prevail over efficiency considerations.

## Acknowledgements

This research was funded by the French Agency for Energy and Environment (ADEME) through project SURORC, contract no. 1181C0066.

## References

- [1] Schuster, A., Karellas, S., Kakaras, E., and Spliethoff, H., 2009. “Energetic and economic investigation of Organic Rankine Cycle applications”. *Applied thermal engineering*, **29**(8-9), pp. 1809–1817.
- [2] Shengjun, Z., Huaixin, W., and Tao, G., 2011. “Performance comparison and parametric optimization of subcritical Organic Rankine Cycle (ORC) and transcritical power cycle system for low-temperature geothermal power generation”. *Applied Energy*, **88**(8), pp. 2740–2754.
- [3] Drescher, U., and Brüggemann, D., 2007. “Fluid selection for the Organic Rankine Cycle (ORC) in biomass power and heat plants”. *Applied Thermal Engineering*, **27**(1), pp. 223–228.
- [4] Invernizzi, C., Iora, P., and Silva, P., 2007. “Bottoming micro-Rankine cycles for micro-gas turbines”. *Applied thermal engineering*, **27**(1), pp. 100–110.
- [5] Karellas, S., and Schuster, A., 2010. “Supercritical fluid parameters in Organic Rankine Cycle applications”. *International Journal of Thermodynamics*, **11**(3), pp. 101–108.
- [6] Chen, Y., Lundqvist, P., and Platel, I. P., 2005. “Theoretical research of carbon dioxide power cycle application in automobile industry to reduce vehicle’s fuel consumption”. *Applied Thermal Engineering*, **25**, pp. 2041–53.
- [7] Chen, Y., Lundqvist, P. J. A., and Platel, I. P., 2006. “A comparative study of the carbon dioxide transcritical power cycle compared with an organic Rankine cycle with R123 as working fluid in waste heat recovery”. *Applied Thermal Engineering*, **25**, pp. 2042–7.
- [8] Saleh, B., Koglbauer, G., Wendland, M., and Fischer, J., 2007. “Working fluids for low-temperature organic Rankine cycles”. *Energy*, **32**(7), pp. 1210–1221.
- [9] Cramer, M., and Kluwick, A., 1984. “On the propagation of waves exhibiting both positive and negative nonlinearity”. *Journal of Fluid Mechanics*, **142**(1), pp. 9–37.
- [10] Hoffren, J., Talonpoika, T., Larjola, J., and Siikoner, T., 2002. “Numerical simulation of real-gas flow in a supersonic turbine nozzle ring”. *Journal of engineering for gas turbines and power*, **124**(2), pp. 395–403.
- [11] Harinck, J., Colonna, P., Guardone, A., and Rebay, S., 2010. “Influence of thermodynamic models in two-dimensional flow simulations of turboexpanders”. *Journal of turbomachinery*, **132**(1).
- [12] Congedo, P. M., Corre, C., and Cinnella, P., 2011. “Numerical investigation of dense-gas effects in turbomachinery”. *Computers & Fluids*, **49**(1), pp. 290–301.
- [13] Rinaldi E, B. A. P. R. C. P., 2013. “Inviscid stator/rotor interaction of a single stage high expansion ratio ORC turbine”. In ASME ORC Conference.
- [14] Thompson, P., 1971. “A Fundamental Derivative in Gas Dynamics”. *Physics of Fluids*, **14**, pp. 1843–1849.
- [15] Cinnella, P., and Congedo, P. M., 2007. “Inviscid and viscous aerodynamics of dense gases”. *Journal of Fluid Mechanics*, **580**, pp. 179–217.
- [16] Setzmann, U., and Wagner, W., 1989. “A new method for optimizing the structure of thermodynamic correlation equations”. *International Journal of Thermophysics*, **10**(6), 11, pp. 1103–1126.
- [17] Tillner-Roth, R., and Dieter Baehr, H., 1994. “An international standard formulation for the thermodynamic properties



- of 1,1,1,2-tetrafluoroethane (HFC-134a) for temperatures from 170 K to 455 K and pressures up to 70 MPa”. *Journal of Physical and Chemical Reference Data*, **23**(5), pp. 657–730.
- [18] Span, R., and Wagner, W., 1996. “A new equation of state for carbon dioxide covering the fluid region from the triple-point temperature to 1100 K at pressures up to 800 MPa”. *Journal of Physical and Chemical Reference Data*, **25**, p. 1509.
- [19] Lemmon, E., and Span, R., 2006. “Short fundamental equations of state for 20 industrial fluids”. *Journal of Chemical & Engineering Data*, **51**(3), pp. 785–850.
- [20] Span, R., and Wagner, W., 2003. “Equations of state for technical applications. I. Simultaneously optimized functional forms for nonpolar and polar fluids”. *International journal of thermophysics*, **24**(1), pp. 1–39.
- [21] Chung, T. H., Lee, L. L., and Starling, K. E., 1984. “Applications of kinetic gas theories and multiparameter correlation for prediction of dilute gas viscosity and thermal conductivity”. *Industrial & engineering chemistry fundamentals*, **23**(1), pp. 8–13.
- [22] Chung, T. H., Ajlan, M., Lee, L. L., and Starling, K. E., 1988. “Generalized multiparameter correlation for nonpolar and polar fluid transport properties”. *Industrial & engineering chemistry research*, **27**(4), pp. 671–679.
- [23] Baldwin, B. S., and Lomax, H., 1978. *Thin layer approximation and algebraic model for separated turbulent flows*, Vol. 257. American Institute of Aeronautics and Astronautics.
- [24] Spalart, P. R., and Allmaras, S. R., 1992. “A one equation turbulence model for aerodynamic flows.”. *AIAA journal*, **94**.
- [25] Cinnella, P., and Congedo, P., 2004. “A Numerical Method for Dense Gas Flow”. *AIAA Journal*, **2137**, p. 34.
- [26] Jameson, A., Schmidt, W., and Turkel, E., 1981. “Numerical solutions of the Euler equations by finite volume methods using Runge-Kutta time-stepping schemes”. *AIAA Journal*, **81**(1259).
- [27] Rezgui, A., Cinnella, P., and Lerat, A., 2001. “Third-order accurate finite volume schemes for Euler computations on curvilinear meshes”. *Computers & fluids*, **30**(7), pp. 875–901.
- [28] Cinnella, P., and Congedo, P., 2005. “Numerical solver for dense gas flows”. *AIAA Journal*, **43**(11), pp. 2458–2461.
- [29] Cinnella, P., and Congedo, P., 2005. “Aerodynamic Performance of Transonic Bethe-Zal’dovich-Thompson Flows past an Airfoil”. *AIAA Journal*, **43**(2), pp. 370–378.
- [30] Roache, P. J., 1998. *Verification and validation in computational science and engineering*. Hermosa Albuquerque.

Table 1. Thermodynamic properties of selected working fluids

	R134a	R245fa	CO <sub>2</sub>
$p_c$ (bar)	40.059	36.51	73.77
$T_c$ (K)	374.21	427.16	304.13
$\rho_c$ (kg/m <sup>3</sup> )	511.9	516.08	467.6
$M_w$ (g/mol)	102.03	134.05	44.01
$\omega$	0.3268	0.3776	0.2239

Table 2. Summary of the considered turbine configurations

Parameters	SUBR134a	SUBR245fa	SUPR134a	SUPR245fa	SUPCO <sub>2</sub>
$p^0$ (bar)	10.4	9.5	47.1	46.9	150.5
$T^0$ (K)	315.51	370.15	396.57	450.43	416.21
Stages	3	3	4	4	4
$Z_{c,in}$	0.80	0.82	0.55	0.46	0.79
$Z_{c,out}$	0.92	0.95	0.85	0.78	0.77
Pressure ratio	6.16	6.16	7.09	7.09	2.33

Table 3. Turbine stage efficiencies for the inviscid model

Stage	SUBR134a	SUBR245fa	SUPR134a	SUPR245fa	SUPCO <sub>2</sub>
1	95.1	92.5	94.6	91.1	98.7
2	94.0	89.6	95.8	92.0	98.3
3	92.9	88.4	95.9	92.4	99.9
4	-	-	98.4	93.6	99.1

Table 4. Turbine stage efficiencies for the B-L model

Stage	SUBR134a	SUBR245fa	SUPR134a	SUPR245fa	SUPCO <sub>2</sub>
1	84.2	78.5	85.7	82.0	89.7
2	84.0	78.4	86.2	82.2	89.9
3	83.9	77.3	86.9	82.6	90.0
4	-	-	87.6	83.0	90.1

Table 5. Turbine stage efficiencies for the S-A model

Stage	SUBR134a	SUBR245fa	SUPR134a	SUPR245fa	SUPCO <sub>2</sub>
1	84.1	80.6	84.7	82.0	89.6
2	83.9	78.8	86.0	82.1	89.8
3	83.4	76.2	86.2	82.2	89.9
4	-	-	87.5	82.3	90.0

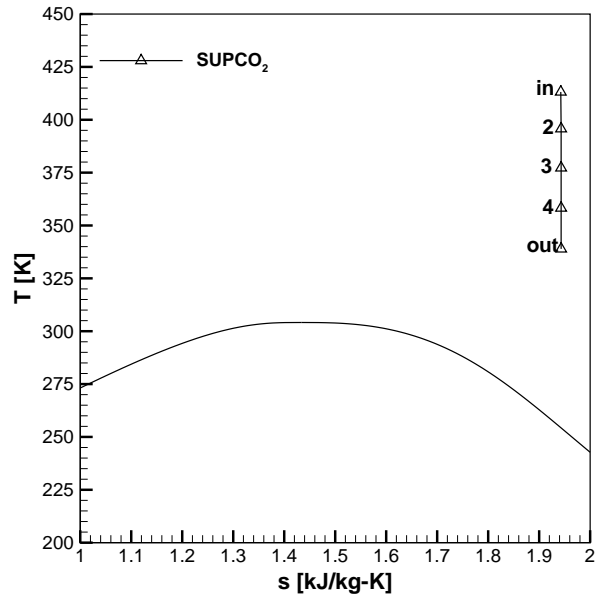


Figure 1. Ideal expansion curve for CO<sub>2</sub>

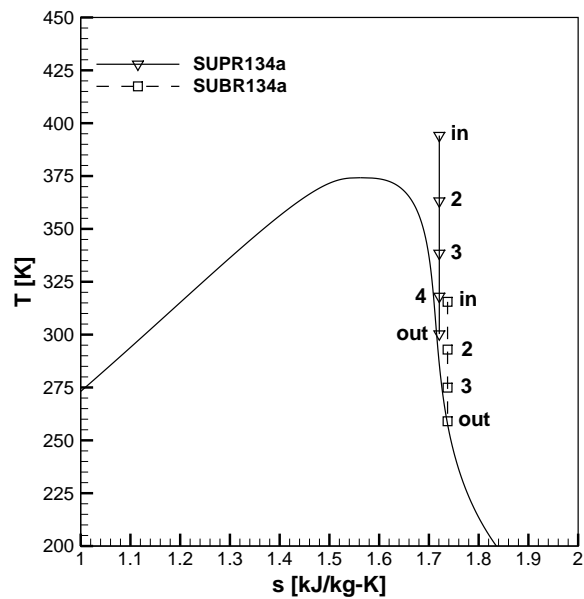


Figure 2. Ideal expansion curves for R134a

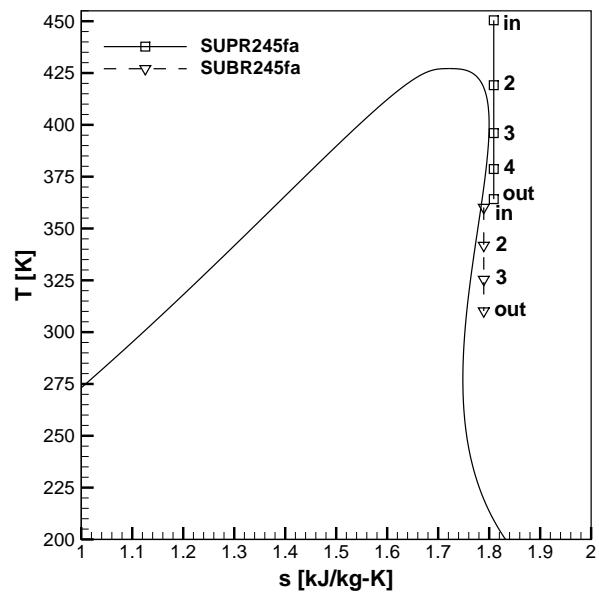


Figure 3. Ideal expansion curves for R245fa

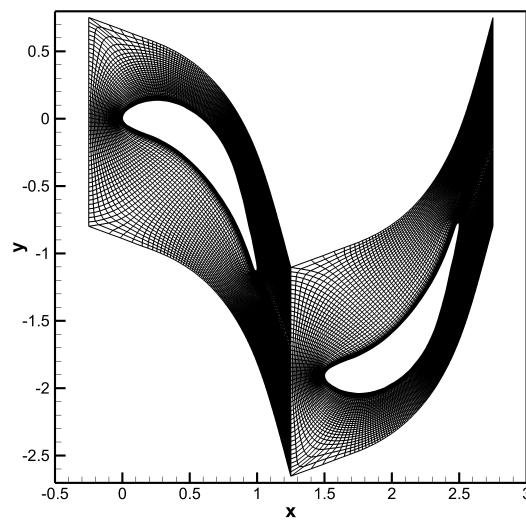


Figure 4. View of the computational grid (384 x 48 cells)

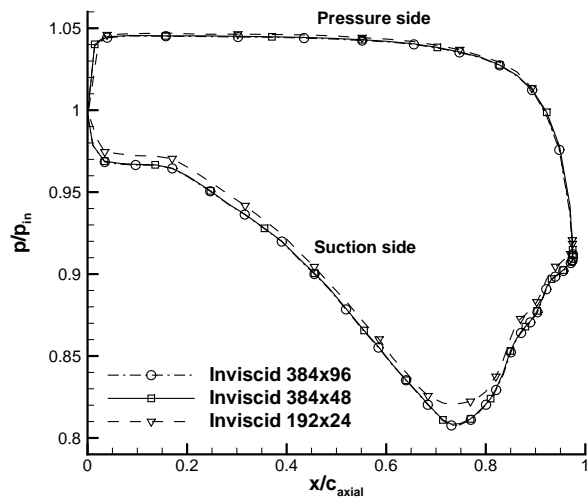


Figure 5. Wall pressure distributions on different grids for case SUPR134a (inviscid simulations)

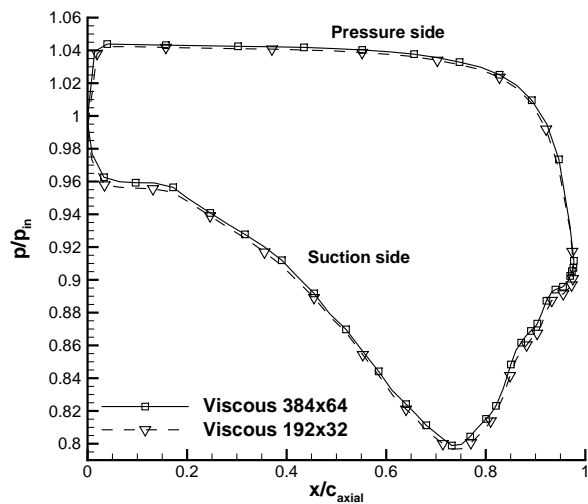


Figure 6. Wall pressure distributions on different grids for case SUPR134a (viscous simulations, Baldwin-Lomax turbulence model)

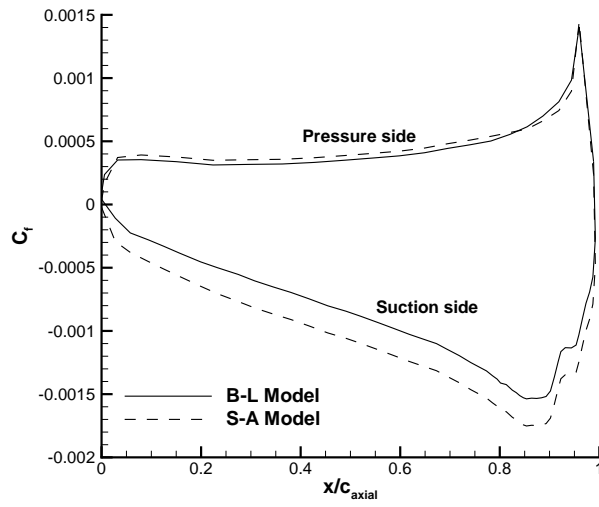


Figure 7. Skin friction coefficient distributions on different grids for case SUPR134a (Baldwin-Lomax turbulence model)

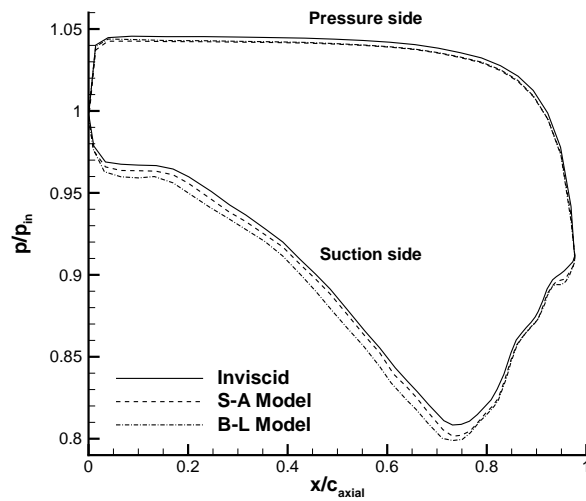


Figure 8. Wall pressure distributions for case SUPR134a (viscous simulations). Effect of the turbulence model

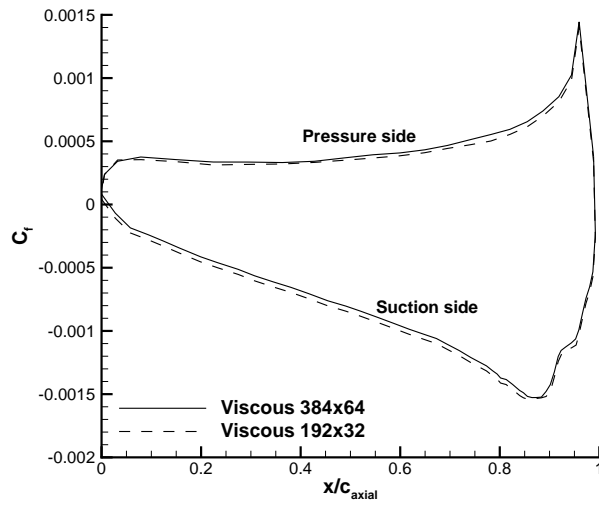


Figure 9. Skin friction distributions for case SUPR134a (viscous simulations). Effect of the turbulence model

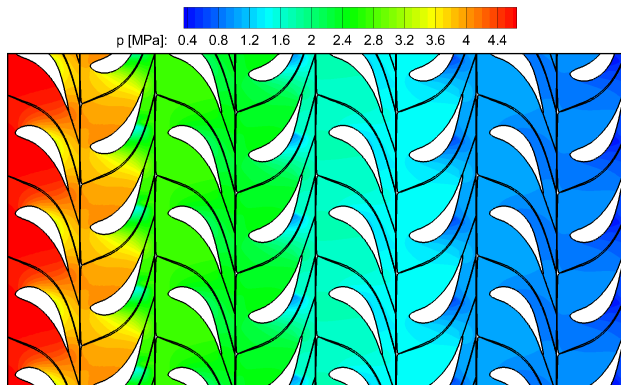


Figure 10. Pressure evolution for SUPR134a case

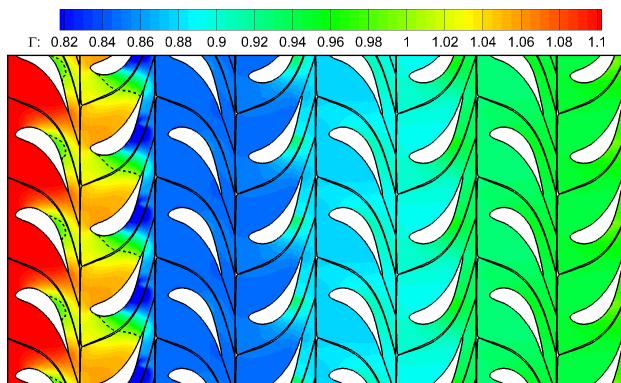


Figure 11. Fundamental Derivative of gas dynamics for SUPR134a case

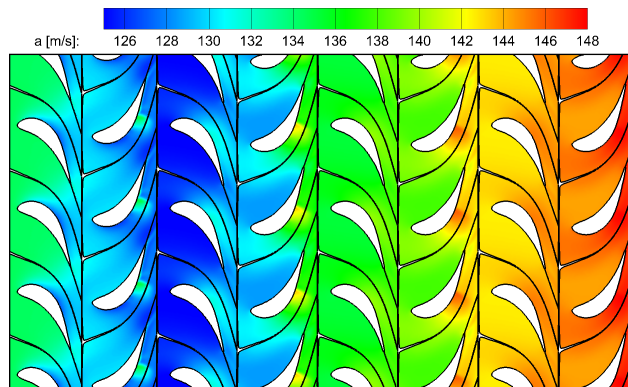


Figure 12. Speed of sound for SUPR134a case

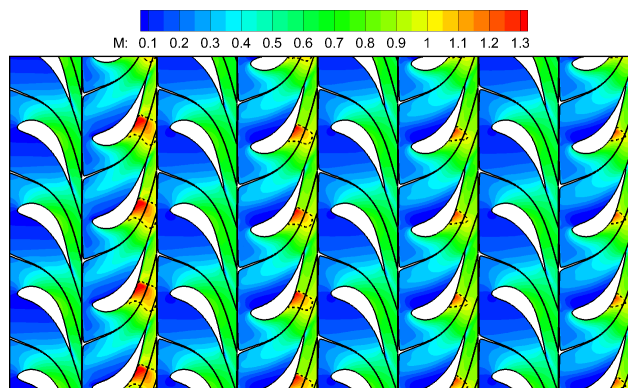


Figure 13. Mach number for SUPR134a case

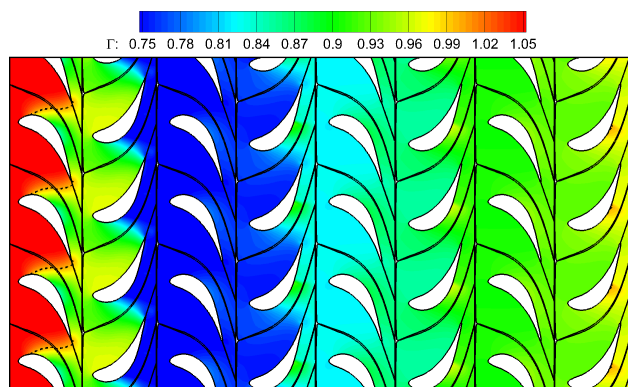


Figure 14. Fundamental Derivative of gas dynamics for SUPR245fa case



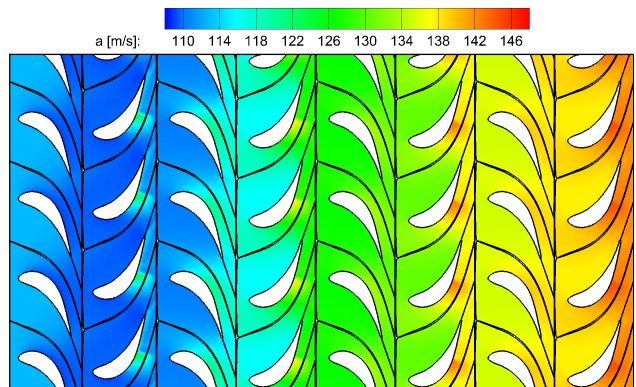


Figure 15. Speed of sound for SUPR245fa case

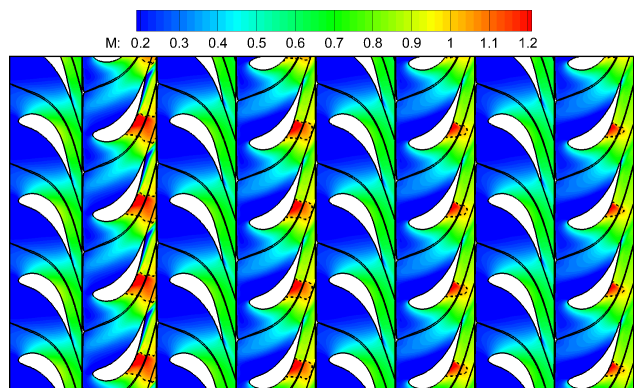


Figure 16. Mach number for SUPR245fa case

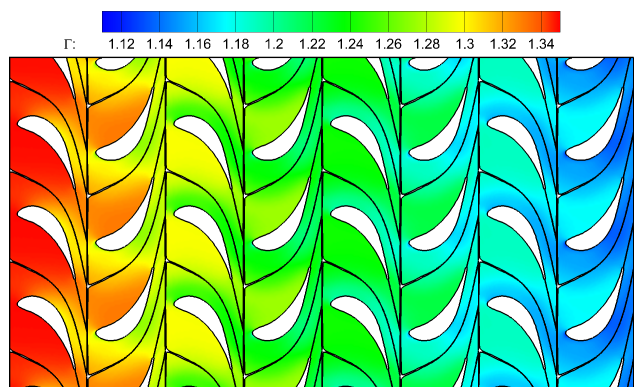


Figure 17. Fundamental Derivative of gas dynamics for SUPCO<sub>2</sub> case

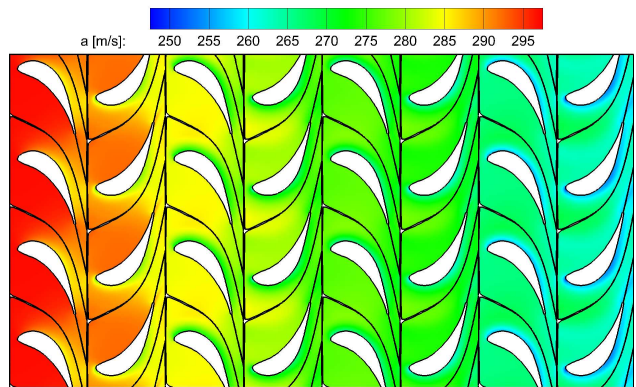


Figure 18. Speed of sound for SUPCO2 case

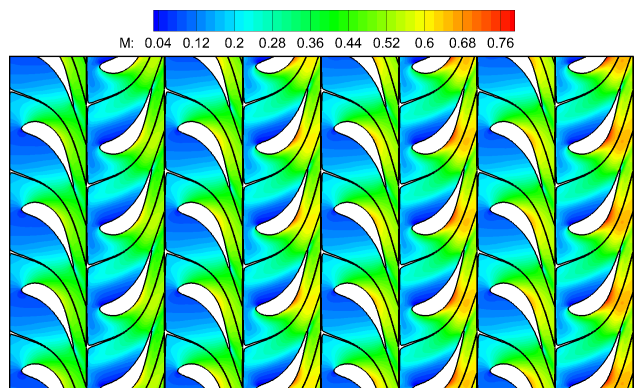


Figure 19. Mach number for SUPCO2 case

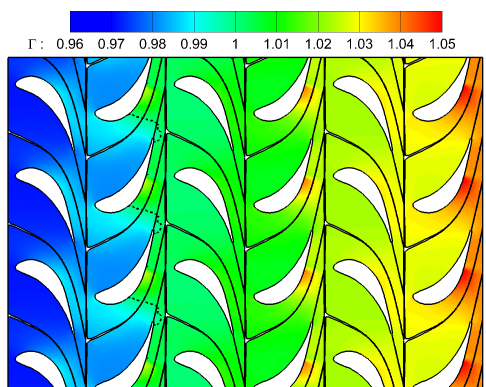


Figure 20. Fundamental Derivative of gas dynamics for SUBR134a case

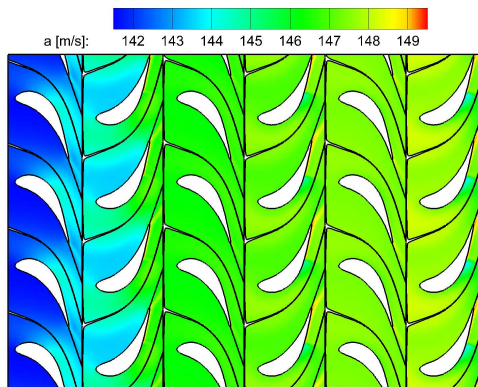


Figure 21. Speed of sound for SUBR134a case

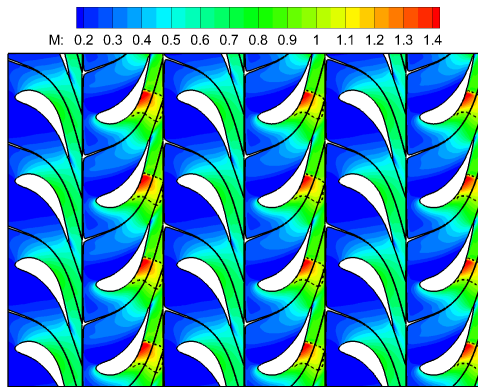


Figure 22. Mach Number for SUBR134a case